ChemComm

COMMUNICATION

View Article Online
View Journal | View Issue

Cite this: *Chem. Commun.*, 2025, **61**, 1144

Received 14th October 2024,
Accepted 5th December 2024

DOI: 10.1039/d4cc05452k

rsc.li/chemcomm

A cost-effective Ca-doped Li_2ZrCl_6 halide solid electrolyte for all-solid-state lithium batteries†

Xingkun Liu, Fanghui Mi and Chunwen Sun *

A cost-effective Ca^{2+}-substituted Li_2ZrCl_6 solid electrolyte (SE) was fabricated by the mechanochemical method, exhibiting high Li^+ conductivity, a wide electrochemical window and excellent compatibility with 4 V-class cathodes. The assembled all-solid-state battery with $LiCoO_2$ achieves a high cycling performance for 150 cycles at 1C with a high-capacity retention of 83.1%.

All-solid-state lithium batteries (ASSLBs) have been widely recognized as a promising candidate for the next-generation battery technology, delivering excellent safety, simpler packaging requirements, longer cycling lifetime and higher energy density by employing lithium metal anodes.[1,2] Solid electrolytes (SEs) play an important role as the critical and indispensable component for ASSLBs.[3] Thus, various types of inorganic SEs including oxides (*e.g.*, $Li_{1.3}Al_{0.3}Ti_{1.7}P_3O_{12}$, $Li_7La_3Zr_2O_{12}$ and $Li_{1.5}Al_{0.5}Ge_{1.5}(PO_4)_3$), sulfides (*e.g.*, $Li_7P_3S_{11}$, Li_6PS_5Cl and $Li_{10}GeP_2S_{12}$) and emerging halides (*e.g.*, Li_3YCl_6, Li_3InCl_6 and $Li_{0.388}Ta_{0.238}La_{0.475}Cl_3$) have been synthesized and explored rapidly.[3–11] Compared to oxide and sulfide SEs, the halide SEs combine both a high redox potential like oxides and excellent mechanical formability similar to sulfides, which makes halide SEs more attractive and promising for application in ASSLBs.[12] Furthermore, a cost-effective Li_2ZrCl_6 (LZC), reported by Ma *et al.*, was successfully synthesized using LiCl and $ZrCl_4$, showing greater potential commercial applications.[13] However, pure LZC possesses a low ionic conductivity of 0.3–0.4 mS cm^{-1}, which needs to be enhanced urgently.[12,14]

Generally, the method of aliovalent substitution of the central metal with different ionic radius cations is recognized as a feasible method to improve Li^+ conductivity *via* changing the Li^+-carrier content and local structural environment.[15] Some studies have shown that the Li^+ conductivity of Li–M–Zr–Cl (M = Sc, Y, Yb, Er, Lu) and Li–M–Hf–Cl (M = In, Y) can be remarkably improved by replacing M^{3+} with tetravalent Zr^{4+} and Hf^{4+}.[16–21] Similarly, Zr-based halide electrolytes were to some extent explored by introducing cations with different valence and ionic radius into LZC, achieving higher Li^+ conductivity and lower active energy.[22] The Li–Zr–M–Cl SEs with pentavalent cations (M = Ta and Nb) were successfully synthesized with excellent ionic conductivity of 1.42 mS cm^{-1} at 25 °C.[23] The M^{3+}-substituted LZC (M = In^{3+}, Sc^{3+}, Fe^{3+}, V^{3+}, Cr^{3+}) were also obtained with higher ionic conductivity.[12,14,24] Thus, divalent-doped LZC SEs with low-cost and high abundance metal elements are worthy of being attempted. The LZC was only explored with Mg^{2+} and Zn^{2+} substitutions until now. Nevertheless, the $Li_{2.1}Zr_{0.95}Mg_{0.05}Cl_6$ possesses a relatively high activation energy of 0.40 eV, which is unamiable under a wide range of temperatures.

Herein, a cost-effective LZC with cheap and high abundance of Ca^{2+} is successfully synthesized *via* the mechanochemical method with an ionic conductivity of 0.58 mS cm^{-1} at room temperature (RT) and the activation energy of 0.33 eV. XRD and bond valence site energy (BVSE) were employed to explore the crystal structure and Li^+ migration pathways. Finally, the solid-state lithium cells with Ca^{2+}-substituted Li_2ZrCl_6 and LCO or scNCM811 cathodes exhibit excellent rate capability and long-term cycling performance.

A series of $Li_{2+2x}Zr_{1-x}Ca_xCl_6$ ($0.0 \leq x \leq 0.2$) SEs were fabricated with different stoichiometric ratios of LiCl, $ZrCl_4$ and $CaCl_2$ through the mechanochemical method at RT. XRD patterns of $Li_{2+2x}Zr_{1-x}Ca_xCl_6$ powders over the range of 0–0.2 are shown in Fig. 1a. Apparently, the XRD pattern of LZC is properly indexed to Li_3YCl_6 (space group = $P\bar{3}m1$, PDF No. 44-0286), which is a trigonal structure with the hexagonal close packing (hcp) arrangement.[12] According to the XRD patterns, there is no $CaCl_2$ impurity observed in the $Li_{2+2x}Zr_{1-x}Ca_xCl_6$ ($0.0 \leq x \leq 0.2$) samples, implying that Ca was successfully introduced into the LZC crystal lattice. Noteworthily, as the amount of Ca increased from 0 to 0.2, a slightly negative shift was observed for the peaks at approximately 16°, 32°, 41° and 50°, which is attributed to the larger ionic radius Ca^{2+} (100 pm)

School of Chemical & Environmental Engineering, China University of Mining and Technology-Beijing, Beijing 100083, P. R. China. E-mail: csun@cumtb.edu.cn

† Electronic supplementary information (ESI) available. See DOI: https://doi.org/10.1039/d4cc05452k

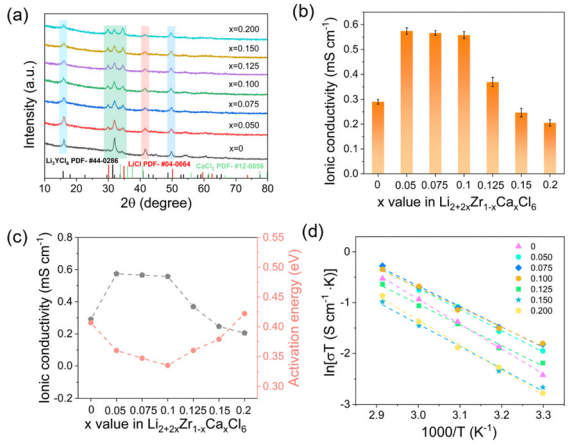

Fig. 1 (a) XRD patterns and (b) ionic conductivity of $Li_{2+2x}Zr_{1-x}Ca_xCl_6$ ($0.0 \leq x \leq 0.2$) SEs. (c) Activation energy (E_a) and ionic conductivity *versus* different Ca contents. (d) Arrhenius plot of Ca^{2+}-substituted LZC SEs at different temperatures from 30 °C to 70 °C.

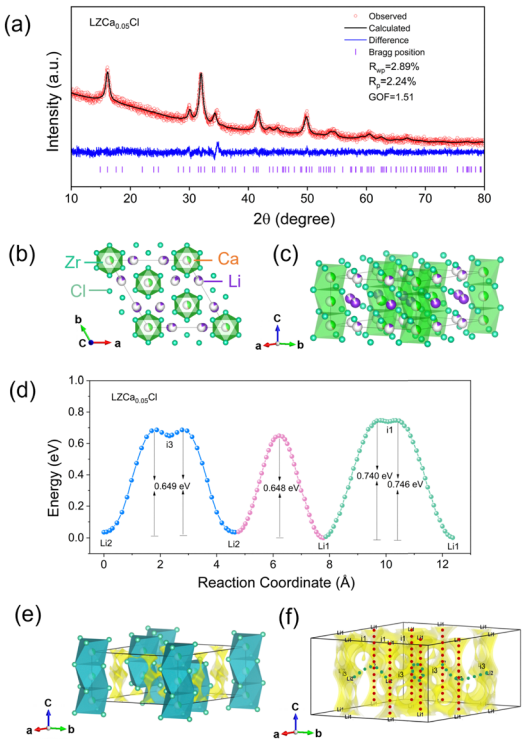

Fig. 2 (a) The Rietveld refinement of the XRD pattern for $LZCa_{0.05}Cl$ at RT. (b) and (c) The crystal structure of $LZCa_{0.05}Cl$ based on the Rietveld refinement result. (d) Energy plots in $LZCa_{0.05}Cl$ for Li^+ migration pathways. (e) The crystal structure of $LZCa_{0.05}Cl$ with Li^+ potential map. (f) Li^+ migration pathway of $LZCa_{0.05}Cl$.

than that of Zr^{4+} (72 pm).[25] However, the composition at $x \geq 0.1$ gradually emerges strong peaks of LiCl at about 30 °C and 34 °C, displaying that the doping content of Ca in LZC is limited, which further explains the sharp decline in Li^+ conductivity at $x \geq 0.1$ in Fig. 1b. The Li^+ conductivity for $Li_{2+2x}Zr_{1-x}Ca_xCl_6$ ($0.0 \leq x \leq 0.2$) shows a basin-shape curve, which is opposite to the shape of the corresponding activation energy curve (Fig. 1c). Thus, the maximum ionic conductivity of 0.58 mS cm^{-1} is obtained at $x = 0.05$ ($LZCa_{0.05}Cl$), while the lowest E_a of 0.33 eV is obtained for $x = 0.1$ ($LZCa_{0.1}Cl$). In addition, the reproducibility of the synthesis method is further confirmed in Fig. S1 (ESI†). Fig. 1d presents the Arrhenius plots of $Li_{2+2x}Zr_{1-x}Ca_xCl_6$ ($0.0 \leq x \leq 0.2$), which are calculated from the EIS at different temperatures from 30 °C to 70 °C (Fig. S2, ESI†). In addition, the electronic conductivities of $Li_{2+2x}Zr_{1-x}Ca_xCl_6$ ($0.0 \leq x \leq 0.2$) are as low as 10^{-9} S cm^{-1}, which satisfies the electron insulation property, as shown in Fig. S3 (ESI†). Besides, the cost of SEs is further discussed in Table S1 (ESI†).

In order to explore the effect of Ca^{2+} substitution on the ionic transport properties in LZC, the bond valence site energy (BVSE) was employed to calculate the Li^+ migration pathway with energy barriers on the basis of Rietveld refinement models.[26,27] According to the above results of XRD and Li^+ conductivity, $LZCa_{0.05}Cl$ was selected for the Rietveld analysis shown in Fig. 2a–c. At the same time, the refined profiles and crystal structure of LZC are shown in Fig. S4a–c (ESI†). In addition, the lattice parameters and atomic coordinates of LZC and $LZCa_{0.05}Cl$ are depicted in Tables S2 and S3 (ESI†). Both phases in the trigonal structure (space group $P\bar{3}m1$) include the arrangement of lithium and zirconium octahedra, in which the $LiCl_6$ octahedra are connected *via* sharing edges or faces with 6h and 6g Wyckoff sites in the crystal structure (Fig. 2c and Fig. S4c, ESI†). The $ZrCl_6$ possesses two types of isolated and sharing-face octahedra. Similarly, calcium octahedra ($CaCl_6$) in $LZCa_{0.05}Cl$ were confirmed by the Rietveld refinement results. There are three different Wyckoff sites (1a, 2d and 1b) for Zr and Ca atoms. However, Ca-substitution significantly adjusts the metal cation occupancy site. In particular, the redistribution of Li-ions was obtained with the increased occupancy of the 6h Wyckoff site, which is beneficial for Li^+ transport.[19] Moreover, compared to the undoped phase, Zr^{4+}/Ca^{2+} centered octahedra expand to larger lattice size in the Ca^{2+}-substituted phase, which is attributed to the larger ionic radius of Ca^{2+} (100 pm). Based on the BVSE analysis, three-dimensional (3D) Li^+ migration pathways are observed for LZC and $LZCa_{0.05}Cl$ and the optimal 1D-Li^+ migration pathway for both is identically the [Li1–Li2] along the *c* direction with the migration barrier of 0.634 eV and 0.648 eV, respectively (Fig. 2d–f and Fig. S4d–f, ESI†). Meanwhile, the migration barrier of the [Li2–i3–Li2] chain between two neighboring *a*–*b* planes obviously decreases from 0.936 eV to 0.649 eV with the Ca^{2+}-substitution LZC, indicating that the [Li2–i3–Li2] chain also becomes relatively favorable for Li^+ transport. However, the migration barrier of the [Li1–i1–Li1] chain within the *a*–*b* plane for $LZCa_{0.05}Cl$ is a little higher (0.746 eV) than that of LZC (0.660 eV). On the whole, the migration barrier for $LZCa_{0.05}Cl$ with 3D Li^+ transport pathways is only 0.746 eV, while the higher migration barrier of 0.936 eV for LZC is required, implying that Ca^{2+} substitution in LZC could effectively reduce the 3D Li^+ migration barrier and improve ionic conductivity. In addition, the content of Li^+ carriers in LZC inevitably increases owing to divalent Ca substitution instead of tetravalent Zr, which is also a vital factor to boost Li^+ conductivity, as reported.[13] To

study this effect, the ionic conductivity of $Li_xZr_{0.9}Ca_{0.1}Cl_{3.8+x}$ ($1.7 \leq x \leq 2.2$) is systemically explored in Fig. S5 (ESI†). It is found that Li^+ conductivity is positively correlated with the content of Li^+ carriers, indicating that the increase of Li carriers is beneficial for enhancing ionic conductivity (additional detailed information can be obtained in Fig. S5, ESI†).

The electrochemical performance of Ca^{2+}-substituted LZC was further evaluated. It should be noted that the electronegativity of Ca (1.0) is much lower than that of Zr (1.33), in addition to being one of the most abundant metal elements in the earth's crust (41 500 ppm).[9] Thus, $LiZCa_{0.1}Cl$ with high Ca doping was selected for subsequent electrochemical measurements, taking into account the overall properties including cost, electronegativity, Li^+ conductivity and activation energy. Firstly, the symmetric Li|$LZCa_{0.1}Cl$|Li cell was assembled to evaluate the compatibility with Li metal. The resistances of the Li|$LZCa_{0.1}Cl$|Li cell gradually increase as the standing time increases from 0 to 12 h (Fig. S6a, ESI†), which is consistent with the overpotential measurement of the Li symmetric cell (Fig. S6b, ESI†). In contrast, the Li symmetric cell using LPSCl as the interlayer between Li metal and halide electrolyte exhibits stable cycling for 250 h at different current densities from 0.05 mA cm^{-2} to 0.3 mA cm^{-2}, indicating that $LZCa_{0.1}Cl$ could maintain good compatibility with LPSCl (Fig. S6c, ESI†). The electrochemical stability window (ESW) of LZC with Ca^{2+}-substitution was also confirmed through linear sweep voltammetry (LSV). Fig. S7 (ESI†) shows that $LZCa_{0.1}Cl$ possesses lower reduction onset potential and higher oxidation onset potential compared to those of LZC, indicating that Ca^{2+} substitution could effectively enlarge ESW to accommodate a wider range of working voltages.

Based on the ESW determined above, Ca^{2+}-substitution LZC is expected to exhibit good compatibility and cycling performance in ASSBs with 4 V-class cathode material. Thus, ASSBs were assembled with $LZCa_{0.1}Cl$ as SE and Li–In alloy as the negative electrode and uncoated-LCO as the positive electrode. Considering the symmetric Li cell above, a thin interlayer of LPSCl was employed to prevent direct contact between the $LZCa_{0.1}Cl$ electrolyte and Li–In anode. As shown in Fig. 3a and Fig. S8a (ESI†), the $LZCa_{0.1}Cl$-based cell shows a larger initial discharge capacity of 144.2 mA h g^{-1} and higher coulombic efficiency of 97.2% at 0.05C, compared to those of the LZC (137.8 mA h g^{-1} and 91.9%). In the same way, the average discharge capacities of the $LZCa_{0.1}Cl$-based cell are 134.9, 125.0, 119.6, 112.5, 100.2 and 77.1 mA h g^{-1} respectively (Fig. 3b and d) when the rate increased from 0.1 to 2C, while the corresponding average discharge capacities of the cell with LZC electrolyte are only 124.0, 104.3, 95.7, 87.7, 78.1 and 66.7 mA h g^{-1}, respectively (Fig. S8b and c, ESI†). After 150 cycles (Fig. 3c), the $LZCa_{0.1}Cl$-based cell still maintains a discharge capacity of 82.9 mA h g^{-1} with a capacity retention of 83.1% at 1C. However, the LZC-based cell exhibits a low discharge capacity of 62.4 mA h g^{-1} with a capacity retention of 79.6% at 1C. Besides, ASSB with $LZCa_{0.1}Cl$ SE still exhibit the capacity retention of 93.5% within 50 cycles under 50 °C in Fig. S9 (ESI†). The difference in long-term cycling, especially for rate capability, implies that the compatibility and stability of

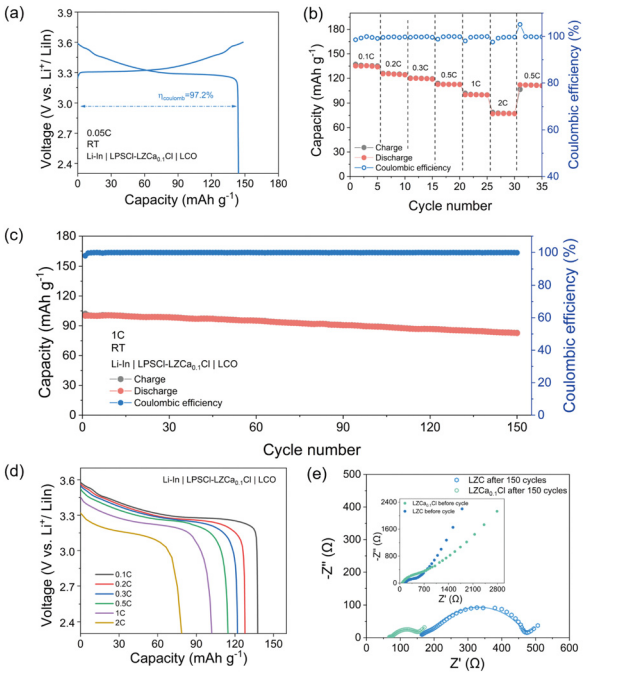

Fig. 3 Electrochemical performance of the Li–In|LPSCl-$LZCa_{0.1}Cl$|LCO cell. (a) Initial charge and discharge curves at 0.05C. (b) Rate capability at 0.1C, 0.2C, 0.3C, 0.5C, 1C, and 2C. (c) Cycling performance at 1C. (d) Discharge curves at 0.1C, 0.2C, 0.3C, 0.5C, 1C, and 2C. (e) Nyquist plots for ASSBs with LZC and $LZCa_{0.1}Cl$ electrolytes before cycling and after 150 cycles.

$LZCa_{0.1}Cl$ SE are much better than that of the LZC electrolyte in ASSBs. EIS measurements for ASSBs after 150 cycles further verify this point. The corresponding Nyquist plots for the LZC and $LZCa_{0.1}Cl$-based cells are shown in Fig. 3e and the fitting results are depicted in Table S4 (ESI†) based on the equivalent circuit model (Fig. S10, ESI†).[28] The intercept in the high frequency region corresponds to the ohmic resistance of SE (R_{SE}). Two semicircles in the Nyquist plots are observed in the middle frequency region and a straight line in the low frequency region. In addition, the first small semicircle represents the interfacial resistance between the Li–In anode and SE (R_{ct1}). Another is related to the interfacial resistance between the cathode and SE (R_{ct2}).[29] Compared to R_{ct1}, R_{ct2} has a more significant influence on cell performance. Apparently, the R_{ct2} of the $LZCa_{0.1}Cl$-based cell (81.7 Ω) is much smaller than that of the LZC-based cell (268 Ω), indicating that the interfacial stability with $LZCa_{0.1}Cl$ is much better than that of LZC. Similarly, ASSBs with the scNCM811 cathode were also further performed in Fig. S11 and S12 (ESI†).

In addition, X-ray photoelectron spectroscopy (XPS) was conducted to investigate the interfacial stability between the LCO cathode and SEs in Fig. 4a and b. The peaks of Cl and Zr in the electrolyte remain unchanged even after undergoing 150 cycles. The peaks corresponding to Ca with low content were also attempted to be detected and the difference is also minimal for the pristine state and after cycling in Fig. S13 (ESI†). The results indicate that the chemical environment remains relatively constant during the cycling process. Likewise, leakage current tests with an extremely high voltage of 4.5 V *vs.* Li^+/Li were conducted to

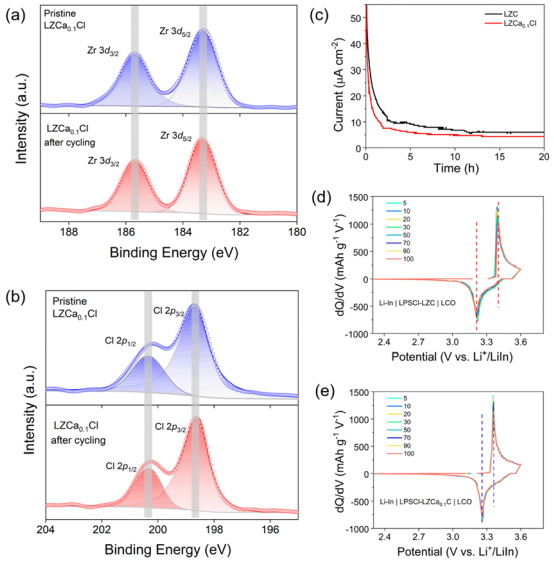

Fig. 4 XPS spectra of the pristine $LZCa_{0.1}Cl$ and LCO-$LZCa_{0.1}Cl$ cathode after 150 cycles: (a) Zr 3d, and (b) Cl 2p. (c) Leakage currents under 4.5 V *vs.* Li^+/Li for 20 h with the LCO cathode. The dQ/dV curves for the LCO cathode with (d) LZC and (e) $LZCa_{0.1}Cl$.

confirm the electrochemical degradation reactions for the electrolytes. The leakage current of $LZCa_{0.1}Cl$ (4.3 μA cm^{-2}) is lower than that of LZC (6.0 μA cm^{-2}), implying that $LZCa_{0.1}Cl$ could effectively inhibit the interfacial side reaction and improve the interfacial stability under high voltage in Fig. 4c. The differential capacity over voltage (dQ/dV) for ASSBs during the cycling process is also analyzed in Fig. 4d and e. Compared to LZC, the $LZCa_{0.1}Cl$-based cell possesses lower anodic and higher cathodic voltages from the 5th to 100th cycles, showing that Ca^{2+}-substituted LZC could effectively maintain excellent voltage and capacity stability. Hence, the ASSBs with $LZCa_{0.1}Cl$ show outstanding high capacity and long-term cycling stability performance.

In summary, a cost-effective Ca^{2+}-substituted LZC was successfully synthesized with higher ionic conductivity and wider electrochemical window. The LZC with Ca doping ($x \leq 0.1$) still maintains the trigonal structure with hcp arrangement. The XRD refinement and BVSE analysis show that Ca doping in LZC could increase the lattice size and effectively reduce the 3D Li^+ migration barrier. Thanks to the high interfacial stability, the ASSBs with Ca^{2+}-substituted LZC electrolyte and uncoated-LCO or scNCM811 cathode exhibit excellent rate capability and cycling performance. We believe that this work provides an available option for practical applications of halide-based ASSBs.

The authors acknowledge the financial support of the National Key R&D Program of China (No. 2023YFE0115800) and the National Natural Science Foundation of China (No. 52472271).

Data availability

The data supporting this article have been included as part of the ESI.†

Conflicts of interest

There are no conflicts to declare.

Notes and references

1 B. Dunn, H. Kamath and J.-M. Tarascon, *Science*, 2011, **334**, 928–935.
2 Q. Yi, W. Zhang, T. Wang, J. Han and C. Sun, *Energy Environ. Mater.*, 2023, **6**, e12289.
3 N. Kamaya, K. Homma, Y. Yamakawa, M. Hirayama, R. Kanno, M. Yonemura, T. Kamiyama, Y. Kato, S. Hama, K. Kawamoto and A. Mitsui, *Nat. Mater.*, 2011, **10**, 682–686.
4 T. Asano, A. Sakai, S. Ouchi, M. Sakaida, A. Miyazaki and S. Hasegawa, *Adv. Mater.*, 2018, **30**, 1803075.
5 H.-J. Deiseroth, S.-T. Kong, H. Eckert, J. Vannahme, C. Reiner, T. Zaiß and M. Schlosser, *Angew. Chem., Int. Ed.*, 2008, **47**, 755–758.
6 X. Li, J. Liang, J. Luo, M. Norouzi Banis, C. Wang, W. Li, S. Deng, C. Yu, F. Zhao, Y. Hu, T.-K. Sham, L. Zhang, S. Zhao, S. Lu, H. Huang, R. Li, K. R. Adair and X. Sun, *Energy Environ. Sci.*, 2019, **12**, 2665–2671.
7 S. Stramare, V. Thangadurai and W. Weppner, *Chem. Mater.*, 2003, **15**, 3974–3990.
8 S. Xiong, Y. Liu, P. Jankowski, Q. Liu, F. Nitze, K. Xie, J. Song and A. Matic, *Adv. Funct. Mater.*, 2020, **30**, 2001444.
9 H. Yamane, M. Shibata, Y. Shimane, T. Junke, Y. Seino, S. Adams, K. Minami, A. Hayashi and M. Tatsumisago, *Solid State Ionics*, 2007, **178**, 1163–1167.
10 Y.-C. Yin, J.-T. Yang, J.-D. Luo, G.-X. Lu, Z. Huang, J.-P. Wang, P. Li, F. Li, Y.-C. Wu, T. Tian, Y.-F. Meng, H.-S. Mo, Y.-H. Song, J.-N. Yang, L.-Z. Feng, T. Ma, W. Wen, K. Gong, L.-J. Wang, H.-X. Ju, Y. Xiao, Z. Li, X. Tao and H.-B. Yao, *Nature*, 2023, **616**, 77–83.
11 T. Yoshinari, R. Koerver, P. Hofmann, Y. Uchimoto, W. G. Zeier and J. Janek, *ACS Appl. Mater. Interfaces*, 2019, **11**, 23244–23253.
12 H. Kwak, D. Han, J. Lyoo, J. Park, S. H. Jung, Y. Han, G. Kwon, H. Kim, S.-T. Hong, K.-W. Nam and Y. S. Jung, *Adv. Energy Mater.*, 2021, **11**, 2003190.
13 K. Wang, Q. Ren, Z. Gu, C. Duan, J. Wang, F. Zhu, Y. Fu, J. Hao, J. Zhu, L. He, C.-W. Wang, Y. Lu, J. Ma and C. Ma, *Nat. Commun.*, 2021, **12**, 4410.
14 H. Zhang, Z. Yu, H. Chen, Y. Zhou, X. Huang and B. Tian, *J. Energy Chem.*, 2023, **79**, 348–356.
15 C. Sun, J. Liu, Y. Gong, D. P. Wilkinson and J. Zhang, *Nano Energy*, 2017, **33**, 363–386.
16 H. Kwak, D. Han, J. P. Son, J. S. Kim, J. Park, K.-W. Nam, H. Kim and Y. S. Jung, *Chem. Eng. J.*, 2022, **437**, 135413.
17 J. Park, D. Han, H. Kwak, Y. Han, Y. J. Choi, K.-W. Nam and Y. S. Jung, *Chem. Eng. J.*, 2021, **425**, 130630.
18 K.-H. Park, K. Kaup, A. Assoud, Q. Zhang, X. Wu and L. F. Nazar, *ACS Energy Lett.*, 2020, **5**, 533–539.
19 K. Tuo, C. Sun, C. A. López, M. T. Fernández-Díaz and J. A. Alonso, *J. Mater. Chem. A*, 2023, **11**, 15651–15662.
20 K. Tuo, F. Yin, F. Mi and C. Sun, *J. Energy Chem.*, 2023, **87**, 12–23.
21 C. Wang, S. Wang, X. Liu, Y. Wu, R. Yu, H. Duan, J. T. Kim, H. Huang, J. Wang, Y. Mo and X. Sun, *Energy Environ. Sci.*, 2023, **16**, 5136–5143.
22 K. Tuo, C. Sun and S. Liu, *Electrochem. Energy Rev.*, 2023, **6**, 17.
23 X.-K. Liu, Y.-X. Zhou, F.-H. Mi, X.-L. Ma and C.-W. Sun, *Energy Storage Mater.*, 2024, **72**, 103737.
24 S. Chen, C. Yu, S. Chen, L. Peng, C. Liao, C. Wei, Z. Wu, S. Cheng and J. Xie, *Chin. Chem. Lett.*, 2022, **33**, 4635–4639.
25 R. D. Shannon, *Acta Crystallogr., Sect., A: Cryst. Phys. Diff., Ttheor. Gen. Crystallogr.*, 1976, **32**, 751–767.
26 H. Chen and S. Adams, *IUCrJ*, 2017, **4**, 614–625.
27 H. Chen, L. L. Wong and S. Adams, *Acta Crystallogr., Sect. B: Struct. Sci.*, 2019, **75**, 18–33.
28 X. Li, M. Liang, J. Sheng, D. Song, H. Zhang, X. Shi and L. Zhang, *Energy Storage Mater.*, 2019, **18**, 100–106.
29 Q. Shao, C. Yan, M. Gao, W. Du, J. Chen, Y. Yang, J. Gan, Z. Wu, W. Sun, Y. Jiang, Y. Liu, M. Gao and H. Pan, *ACS Appl. Mater. Interfaces*, 2022, **14**, 8095–8105.